Morphology of amorphous $Fe_{91}Zr_9/Al_2O_3$ multilayers: Dewetting and crystallization

A. Liebig,[1] P. T. Korelis,[1] H. Lidbaum,[2] G. Andersson,[1] K. Leifer,[2] and B. Hjörvarsson[1,*]
[1]*Department of Physics, Uppsala University, Box 530, SE-75121 Uppsala, Sweden*
[2]*Department of Engineering Sciences, Uppsala University, Box 534, SE-75121 Uppsala, Sweden*
(Received 26 January 2007; published 5 June 2007)

Amorphous $Fe_{91}Zr_9/Al_2O_3$ multilayers grown by magnetron sputtering have been studied using x-ray reflectometry, x-ray diffraction, Rutherford backscattering spectrometry, and transmission electron microscopy. It could be demonstrated that on the interface between the $Fe_{91}Zr_9$ and the Al_2O_3, crystalline grains are formed, that for very small repetition thicknesses destroy the periodicity of the multilayers by accumulative roughness. Understanding these effects would enable substantial improvement of the quality of nanolaminated amorphous layers.

DOI: 10.1103/PhysRevB.75.214202 PACS number(s): 71.20.Lp, 71.23.Cq, 61.10.Kw, 68.37.Lp

I. INTRODUCTION

Ferromagnet/insulator heterostructures have attracted considerable interest, particularly due to the possible use of oxide layers as barriers in magnetic tunnel junctions.[1] Although substantial efforts have been invested, there still remain a number of unresolved questions with respect to the processes involved. The comparison between experimental and theoretical efforts relies on realistic description of the structural parameters, as well as the scattering processes at interfaces. Exploration of the structural properties of such structures is therefore of large importance.

The use of single crystals as building blocks is one of the possible routes to obtain structural and interface perfection. However, crystalline interfaces always suffer from the presence of atomic steps, leading to strain fields and variation in the layer thicknesses. Thus, the removal of atomic steps would remedy one of the biggest obstacles in the production of such structures. The obvious route would be to grow the layers in a phase-locked way, ensuring the complete formation of the evolving layer before starting with the second one. Although this approach is conceptually simple, the practical implementation is far from trivial.

Another route which eliminates the presence of atomic steps is the complete removal of crystallinity. Thus, if amorphous layers are used as building blocks, there will be no atomic terraces at the interfaces, as there are no atomic planes. Consequently, there will be no variation in thickness originating from atomic steps of the interface region. The interest for amorphous ferromagnets, such as FeCoB metallic glasses,[2] has also increased substantially due to the low coercivity and high saturation magnetization. These features are highly interesting in the current context, both from fundamental and applied points of view.[3,4]

Since many amorphous materials are metastable, recrystallization can take place at elevated temperatures. The stability and the structural modifications upon annealing have been investigated by several groups.[5,6] The stability of amorphous heterostructures can differ widely due to interfacial effects. For metal-metal systems, inhomogeneous interfaces can stabilize an amorphous phase while the bulk already crystallizes.[7,8] On the other hand, at a crystalline-liquid interface, lattice-matched underlayers can initiate the formation of ordered regions in the liquid.[9,10] For semiconductors, crystallization induced by defects in the substrate has also been observed.[11] Thus, for successful use of amorphous multilayers, substantial efforts have to be invested in exploring routes for tailoring the atomic structure of the interface.

Here, we report a study of $Fe_{91}Zr_9/Al_2O_3$ multilayers grown on amorphous silicon oxide. Aluminum oxide (Al_2O_3) grows amorphous at room temperature,[12] as does $Fe_{91}Zr_9$.[13] This material combination appears, therefore, to be highly suitable for obtaining amorphous multilayers consisting of metallic and insulating layers. Iron zirconium alloys in this concentration range become ferromagnetic at approximately 200 K (see, e.g., Refs. 14–16). Therefore, the range below and above the magnetic transition is easily accessible without the need to warm up, risking thermally induced structural changes. We will address the effect of interfaces on the resulting structure and prove the importance of dewetting in the growth process.

II. EXPERIMENT AND RESULTS

A. Growth and preparation

The samples were grown in an ultrahigh vacuum system by magnetron sputtering. The argon pressure used was 0.4 Pa, aluminum oxide was deposited from an rf source, and the iron zirconium alloy was grown by codeposition from two dc sources. Si(001) wafers either thermally oxidized or with natural oxide layers were used as substrates. All the growth sequences started with an aluminum oxide layer, ensuring similar growth conditions for the metallic layers. To prevent oxidation, the sample stacks ended with aluminum oxide layers as capping.

The nominal thicknesses of the Al_2O_3 layers were in the range of 10–20 Å for all the samples. Thicknesses of the metallic $Fe_{91}Zr_9$ layers were varied from 12 to 130 Å. The number of multilayer repetitions was varied between 10 and 30 to achieve an equivalent total thickness. All the samples were grown at room temperature.

For transmission electron microscopy (TEM), samples were prepared using dimple grinding techniques. The samples were polished to electron transparency using grazing incidence ion milling.

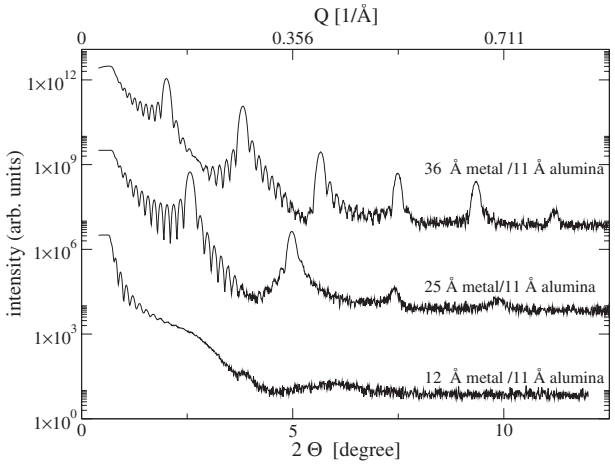

FIG. 1. X-ray reflectivity curves for samples with varied metal layer thickness as indicated. Increase of metal layer thickness leads to higher-order multilayer peaks. Scans are offset for clarity.

B. Structural characterization

The structural characterization was performed utilizing both real and reciprocal space techniques.

X-ray reflectometry (XRR) and x-ray diffractometry (XRD) were used to characterize all the samples, providing information about the layer structure and the atomic arrangement, respectively. The XRR scans were done on a Siemens D5000 diffractometer in Bragg-Brentano focusing geometry with Cu $K\alpha$ radiation ($\lambda = 1.54$ Å) and a secondary monochromator. Three scans for samples with different metal layer thicknesses, presented in Fig. 1, reveal a striking change in structure: the sample with the thickest metal layer shows pronounced multilayer peaks up to the sixth order. This corresponds to very well defined thicknesses of the layers. The total thickness of the stack is well defined, as seen by the extension of the Kiessig fringes which are observed up to nearly 8° in 2θ. Simulation of the XRR data using the GENX software[17] employing Parratt's algorithm[18] yields an interfacial roughness value of approximately 2.5 Å or 7% of the layer thickness for the FeZr layer. The good quality of the multilayer structure for this sample, as well as for those with thicker metal layers, is apparent in the TEM. As an example

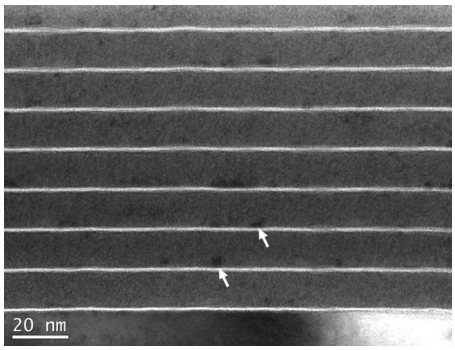

FIG. 2. Bright field TEM micrograph of sample with 130 Å FeZr and 18 Å Al_2O_3 layers on Si with native oxide. Grains within the FeZr appear preferentially at the lower interfaces (arrows).

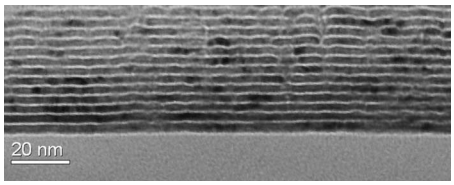

FIG. 3. Bright field TEM micrograph of sample with 25 Å FeZr and 11 Å Al_2O_3 layers. An increased waviness and variation in thickness of the layers as compared to the sample in Fig. 2 is apparent.

of this, a bright field micrograph recorded with a FEI Tecnai F30ST at 300 kV is presented in Fig. 2.

For thinner metal layers, however, the situation (Fig. 1) changes: the higher-order multilayer peaks are much weaker, or, in the case of the thinnest metal layer, entirely absent. For the sample with 25 Å metal, the roughness is determined to be 4 Å or 18% of the layer thickness. For the thinnest metal layer, a meaningful simulation is no longer possible.

When regarding the TEM results, the structural change is apparent. The bright field micrograph shown in Fig. 3 (using a JEOL JEM-2000FXII) reveals strong variation of the layer thickness and increased waviness. The weak or even missing Kiessig fringes in the XRR illustrate the propagation of the waviness, influencing the variation in the overall total thickness of the film.

Additional features, appearing as nanometer sized dark contrasts, are observed in the TEM images (Figs. 2 and 3). Using the Tecnai microscope in high-resolution mode (Figs. 4 and 5) reveals structural order within these regions.

In thicker metal layers (Figs. 2 and 5), most crystallites seem to appear at the lower interface and be limited in size. Thus, the oxide interface appears to induce crystallization during the initial growth of the layers. However, when the metal thickness is comparable to the size of the grains (approximately 30–40 Å), these extend through the entire layer (Fig. 4). For even thinner layers, the multilayer structure becomes unstable with roughness accumulating from layer to layer, as described above.

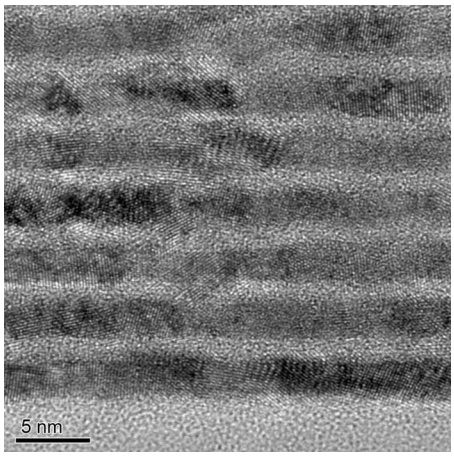

FIG. 4. High-resolution TEM micrograph of the sample shown in Fig. 3 (25 Å FeZr and 11 Å Al_2O_3 layers). Crystalline grains extending through the entire thickness of the metal layer are clearly seen.

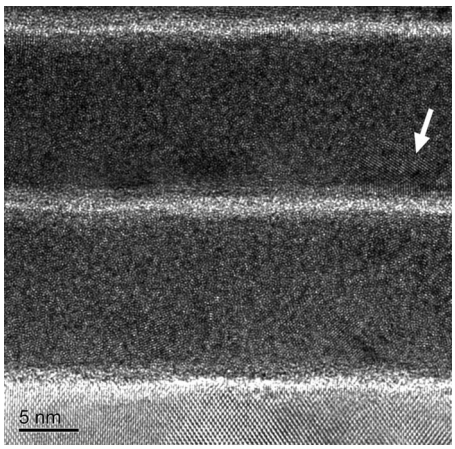

FIG. 5. High-resolution TEM micrograph of the sample shown in Fig. 2 (130 Å FeZr and 18 Å Al_2O_3 layers). Local crystallization appears, mainly on the lower interfaces, as indicated by the arrow.

To complement the local TEM measurements, x-ray diffraction, probing a much larger part of the sample, was used. This was done on a Philips X'pert diffractometer with a primary Göbel mirror and a secondary flat-crystal graphite monochromator suppressing iron fluorescence radiation from the sample. The used wavelength (Cu $K\alpha$, $\lambda=1.54$ Å), however, limits the accessible Q range.

The scans (Fig. 6) show increased intensity with decreased Q value from the amorphous material, as well as a wide peak at $2\theta \approx 43.5°$. While we expect diffracted intensity close to this position (compare Ref. 19), this peak is too narrow to result from the structure factor of the amorphous material. Its position corresponds to the Fe(110) position and its width gives a coherence length between 10 and 20 Å. Albeit the scans do not cover the diffuse peak at lower Q completely, the change in relative intensity between the amorphous contribution and the peak at $2\theta \approx 43.5°$ is striking. For the single layer, the crystalline peak appears only as

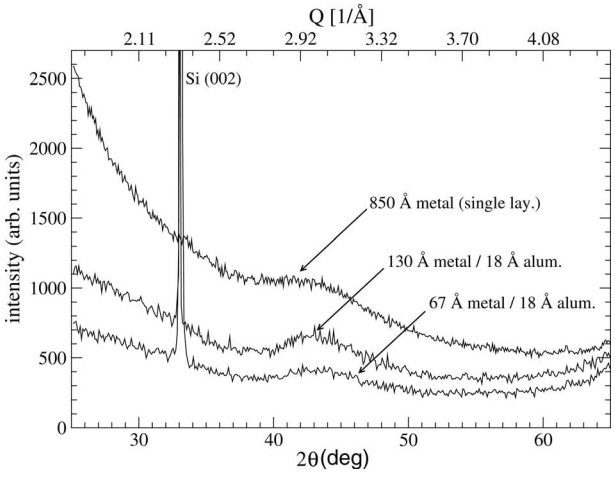

FIG. 6. Symmetric scans of samples with different interface densities. Sample compositions are given in the figure. The increase in intensity toward lower Q values is consistent with the diffuse ring in the electron diffraction pattern in Fig. 7. The forbidden Si(002) reflection from the substrate is also marked.

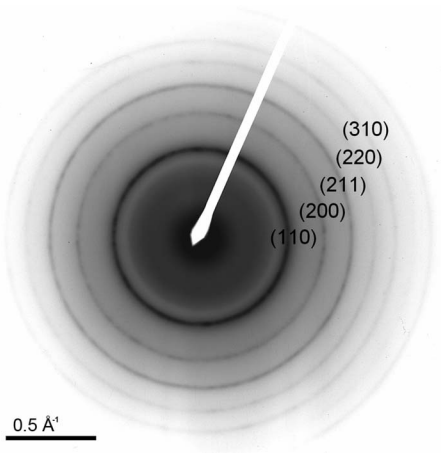

FIG. 7. Selected area electron diffraction pattern (top-view geometry) of a sample with 50 Å thick FeZr layers. Rings correspond to polycrystalline iron and diffuse rings are from the amorphous material. Indices of diffracting lattice planes are indicated. The scale was calibrated using the Si substrate of the same sample.

a shoulder on the diffuse peak, for the sample with the highest interface density, the diffuse peak is much weaker.

Therefore, it is equally possible to link the fraction of crystalline FeZr to the interfaces by the XRD measurements.

To study the influence of the crystallites, magneto-optical Kerr effect (MOKE) measurements at room temperature were performed. For completely amorphous iron zirconium alloys in this concentration range, the Curie temperature would be approximately 200 K,[14–16] as mentioned above. These samples, however, show a ferromagnetic signal even at room temperature, proving the existence of a crystalline fraction. Magnetic measurements as a function of temperature (both MOKE and superconducting quantum interference device magnetometry) yield for this materials, depending on the sample, a shoulder or a tail on the magnetization versus temperature curve, showing the existence of two phases with different Curie temperatures. Quantitative interpretation of these measurements, however, proved to be challenging, possibly due to the polarization of the matrix by superparamagnetic clusters. A more detailed study will be published separately.[20]

Selected area electron diffraction (SAED) was used to determine the lattice parameter of the crystalline enclosures. The SAED yields higher signal-to-noise ratio than the performed x-ray measurements and accesses easily a large Q range. It was, therefore, preferred over the XRD measurements, with which it is in good agreement.

Since the crystallites are preferentially located at the interfaces, a sample with thin metallic layers, resulting in a high interface density, seems to be preferable here. On the other hand, wavy or even discontinuous layers could introduce other effects. Therefore, a sample with medium metal layer thickness (50 Å) was prepared in top-view geometry to maximize the volume of the film that is illuminated in the measurement. The diffraction pattern shown in Fig. 7 corresponds to an expanded $\alpha-$Fe lattice ($a=2.91$ Å as compared to $a_{Fe}=2.87$ Å).

Such lattice expansions are often interpreted by assuming a linear relation between atomic concentration and lattice

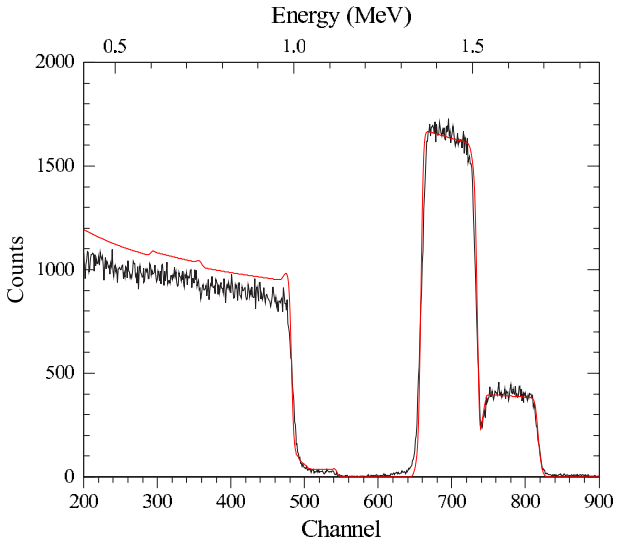

FIG. 8. (Color online) RBS spectrum of a sample with 130 Å metal and 18 Å aluminum oxide, repeated ten times. The simulated curve corresponds to the composition of $Fe_{91}Zr_9$. For the silicon substrate, slight channeling results in lower intensity than expected from the simulation.

parameter. This relations is known as Vegard's law. It is not always a valid approximation. Especially for metallic solid solutions, substantial deviations are observed (see, e.g., Refs. 21 and 22). However, for the incorporation of zirconium into α-iron it has been found to hold.[23] The expansion is then consistent with an incorporation of $(6\pm2)\%$ of Zr into the crystallites. This corresponds nearly to the maximum amount of Zr that can be incorporated into iron without amorphization.[13,23,24] Before discussing the significance of this observation, we need to address the average composition of the FeZr layers.

The composition of the samples was determined by Rutherford backscattering spectrometry (RBS). The RBS measurements (*ex situ*) were performed with single charged He^+ ions at a primary beam energy of 2.00 MeV, at a scattering angle of 160°. The RUMP software package from CGS,[25] utilizing the algorithm described by Doolittle,[26] was used for the analysis of the RBS data.

Typical RBS results are shown in Fig. 8. While the resolution is inherently insufficient to resolve the individual layers, the average composition ratio between iron and zirconium can readily be obtained. The zirconium content in the metal layers was determined to be between 9.3% and 9.6%, consistent with the intended composition. Thus, the Zr concentration of the crystallites is substantially lower than the average of the layers. Phase separation at the length scale of the crystallites is, therefore, apparent, resulting in compositional modulation within the metallic layers.

III. DISCUSSION

Metal films on oxide layers often grow in islands (see, e.g., Ref. 27), initially forming discontinuous layers. The origin of the discontinuous growth lies in the relatively high energy of the metal-oxide interface. Thus, the total energy is reduced by an increase of the metal-vacuum interface area, decreasing the effective interface area between the metal and the oxide. For higher coverages, when the holes between the islands have eventually been filled, the surface energy can give rise to a smoothening process, resulting in a well defined thickness above a critical thickness of the layers. This effect can have pronounced influence on the variation in the layer thickness when depositing metal-oxide multilayers. For example, if the oxide layer is deposited on the discontinuous metal film, the metal will be locked in the oxide structure as small particles corresponding to the island size. This feature has, for example, been observed by Soroka *et al.* in the growth of polycrystalline Permalloy/amorphous aluminum oxide multilayers,[28] where the Permalloy forms small particles when the nominal layer thickness is below a critical value.

In the current results, the TEM and x-ray investigations clearly show an interface related crystallization. The appearance of separated crystallites in the TEM images, preferentially at the lower interfaces, clearly supports the view of phase separation in the initial growth of the metal on the oxide layer. These regions have different chemical compositions, as compared to the average composition of the layers. Their initial growth as islands results in thickness variations and strong accumulative roughness for samples with short repeat distance.

The presence of island growth mode is supported by the x-ray reflectivity data, as well as the interface energies found in the literature.[29] However, the interpretation is complicated by the presence of two phases, the low-Zr crystalline phase and the high-Zr regions which are amorphous. Since the crystal growth apparently peters out in the later stages of growth, it can be argued that the phase separation and the crystallization must occur during the initial stages of growth, when the film is still discontinuous. Thus, there appears to be a critical range for the growth of nanocrystallites starting at the interfaces, possibly limited by the increase in the Zr activity due to the increase in local Zr concentration.

We can view the film growth as a three step process: first, nucleation of small clusters by agglomeration of single atoms; second, formation of island grains, and third, formation of a continuous film after complete metal coverage. Following the argumentation above, the phase separation must occur during the first, or possibly the first two, steps.

The initial nucleation phase is the most difficult one to access, since the growth processes are occurring in extreme nonequilibrium conditions: deposited atoms hit the surface with 1–3 eV, corresponding to more than 12 000 K, while the substrate is kept at room temperature. However, an impacting atom dissipates its energy extremely quickly,[30,31] within very few oscillation periods after the impact. We argue, therefore, that, despite the strong overall nonequilibrium conditions, an adatom can, shortly after adsorption, be viewed as being close to a local equilibrium with the surface itself. Therefore, it should be possible to use a thermodynamical description as a rough approximation.

At thermal equilibrium, the growth rate of the initial clusters—the rate at which single atoms join clusters of size n—depends strongly on the activation energy for surface diffusion (see, e.g., Ref. 32) as

$$\Gamma_n^+ = \sigma_n N_1 a \nu \exp\left(\frac{Q_D}{kT}\right), \quad (1)$$

where σ_n is the capture width of the cluster, N_1 the number of single atoms on the surface, a the separation between the clusters, ν the attempt frequency, and Q_D the activation energy for surface diffusion.

If Q_D is different for the two elements (Fe and Zr), the one with the higher diffusion rate will more readily form clusters, when energetically favorable. The activation energy for the diffusion can be approximated by scaling of the adsorption energy. The free-energy gain for noble and transition metals can be estimated from the sublimation enthalpy[29,33] using

$$\Delta H_{ads,avg} \approx -(0.77 \pm 0.09)\Delta H_{subl}. \quad (2)$$

The sublimation enthalpy for iron and zirconium is 416.3 and 608.8 kJ/mol, respectively.[34] Therefore, it can be expected that Fe atoms join initial clusters with a higher rate than Zr atoms at a given temperature, resulting in changes of the local chemical composition.

In the second step, further growth of the nucleated grains takes place. Since the $\alpha-$Fe phase cannot incorporate more than 7% Zr, a grain either has to grow amorphous, or the excess Zr is accumulating on the surface, until it reaches a concentration that inhibits further crystal growth. Therefore, the phase separation and crystallization are linked to the nucleation of the initial islands.

IV. CONCLUSIONS

The results clearly show the presence of dewetting induced phase separation at $Al_2O_3/Fe_{91}Zr_9$ interfaces. This strongly affects the possibility of forming fully amorphous metal-oxide junctions at room temperature. This effect has even more devastating influence on the formation of multilayers, as the accumulative roughness causes complete loss of periodicity after only a few repeats. The formation of crystallites is, therefore, causing a severe challenge during the growth of amorphous metal insulator heterostructures.

The initial phase separation is induced by the presence of the interface, on which nucleation centers for crystal growth are formed. This effect can be lessened by reducing the surface mobility by, for example, growing the films at lower temperatures. Another possibility is to alter the interface energy by the choice of the constituents. However, this could limit the choice of materials in an undesired way.

The interplay between dewetting and phase separation has attracted considerable attention within the field of polymer science (examples include Refs. 35 and 36) but seems to have received little notice in the field of thin metallic films. The growth of materials with large differences in the interface energies calls for better theoretical description, which poses a considerable challenge as the minimization of the total energy of amorphous structures is almost impossible within the framework of first-principles calculations.

ACKNOWLEDGMENTS

Financial support by Vetenskapsrådet is gratefully acknowledged. The authors would like to thank Andrew Wildes, ILL, Grenoble, for inspiring discussions.

*Corresponding author. FAX: +46(0)18-4713524. Electronic address: bjorgvin.hjorvarsson@fysik.uu.se

[1] J. S. Moodera, L. R. Kinder, T. M. Wong, and R. Meservey, Phys. Rev. Lett. **74**, 3273 (1995).
[2] D. D. Djayaprawira, K. Tsunekawa, M. Nagai, H. Maehara, S. Yamagata, N. Watanabe, S. Yuasa, Y. Suzuki, and K. Ando, Appl. Phys. Lett. **86**, 092502 (2005).
[3] Y. Yoshizawa, S. Oguma, and K. Yamauchi, J. Appl. Phys. **64**, 6044 (1988).
[4] G. Herzer, Mater. Sci. Eng., A **133**, 1 (1991).
[5] X. D. Liu, X. B. Liu, and Z. Altounian, J. Non-Cryst. Solids **351**, 604 (2005).
[6] N. Zárubová, N. Moser, and H. Kronmüller, Mater. Sci. Eng., A **151**, 205 (1992).
[7] U. Herr, Adv. Eng. Mater. **3**, 889 (2001).
[8] U. Herr, Contemp. Phys. **41**, 93 (2000).
[9] A. Bonissent, J. Finney, and B. Mutaftshiev, Philos. Mag. B **42**, 233 (1980).
[10] A. J. C. Ladd and L. V. Woodcock, J. Phys. C **11**, 3565 (1978).
[11] J. Y. Wang, D. He, Y. H. Zhao, and E. J. Mittemeijer, Appl. Phys. Lett. **88**, 061910 (2006).
[12] J. M. Schneider, W. D. Sproul, and A. Matthews, Surf. Coat. Technol. **94-95**, 179 (1997).
[13] U. Herr, H. Ippach, and K. Samwer, Appl. Phys. Lett. **75**, 1730 (1999).
[14] A. R. Wildes, J. R. Stewart, N. Cowlam, S. Al-Heniti, L. F. Kiss, and T. Kemény, J. Phys.: Condens. Matter **15**, 675 (2003).
[15] D. H. Ryan, J. M. D. Coey, E. Batalla, Z. Altounian, and J. O. Ström-Olsen, Phys. Rev. B **35**, 8630 (1987).
[16] D. Kaptás, T. Kemény, L. F. Kiss, L. Gránásy, J. Balogh, and I. Vincze, J. Non-Cryst. Solids **156-158**, 336 (1993).
[17] M. Björck, Ph.D. thesis, Uppsala, 2007 (http://publications.uu.se/abstract.xsql?dbid=3D7886); M. Björck and G. Andersson (unpublished).
[18] L. G. Parratt, Phys. Rev. **95**, 359 (1954).
[19] H. S. Chen, K. T. Aust, and Y. Waseda, J. Non-Cryst. Solids **46**, 307 (1981).
[20] P. T. Korelis (unpublished).
[21] B. D. Cullity, *Elements of X-ray Diffraction*, 2nd ed. (Addison-Wesley, Reading, MA, 1978), Chap. 12, p. 376.
[22] A. R. Denton and N. W. Ashcroft, Phys. Rev. A **43**, 3161 (1991).
[23] U. Herr, H. Geisler, H. Ippach, and K. Samwer, Phys. Rev. B **59**, 13719 (1999).
[24] *Binary Alloy Phase Diagrams*, 2nd ed. edited by T. B. Massalski, H. Okamoto, P. R. Subramanian, and L. Kacprzak (ASM International, Materials Park, Ohio, 1990).
[25] M. Thompson, RUMP, RBS analysis and simulation package, version (4.00(beta), 2004) (http://www.genplot.com).

[26] L. R. Doolittle, Nucl. Instrum. Methods Phys. Res. B **15**, 227 (1985).
[27] M. L. Colaianni, P. J. Chen, and J. J. T. Yates, Surf. Sci. **238**, 13 (1990).
[28] I. L. Soroka, V. Stanciu, J. Lu, P. Nordblad, and B. Hjörvarsson, J. Phys.: Condens. Matter **17**, 5027 (2005).
[29] C. T. Campbell, Surf. Sci. Rep. **27**, 1 (1997).
[30] B. McCarroll and G. Ehrlich, J. Chem. Phys. **38**, 523 (1963).
[31] A. V. Plyukhin and J. Schofield, Phys. Rev. E **65**, 026603 (2002).
[32] D. Walton, J. Chem. Phys. **37**, 2182 (1962).
[33] S. H. Overbury, P. A. Bertrand, and G. A. Somorjai, Chem. Rev. (Washington, D.C.) **75**, 547 (1975).
[34] *CRC Handbook of Chemistry and Physics*, 86th ed., edited by D. R. Lide (CRC, Boca Raton, PL, 2005).
[35] P. Müller-Buschbaum, E. Bauer, O. Wunnicke, and M. Stamm, J. Phys.: Condens. Matter **17**, S363 (2005).
[36] R. Yerushalmi-Rozen, T. Kerle, and J. Klein, Science **285**, 1254 (1999).